

Progressive Adversarial Semantic Segmentation

Abdullah-Al-Zubaer Imran and Demetri Terzopoulos

Computer Science Department
University of California, Los Angeles, California, USA

Abstract—Medical image computing has advanced rapidly with the advent of deep learning techniques such as convolutional neural networks. Deep convolutional neural networks can perform exceedingly well given full supervision. However, the success of such fully-supervised models for various image analysis tasks (e.g., anatomy or lesion segmentation from medical images) is limited to the availability of massive amounts of labeled data. Given small sample sizes, such models are prohibitively data biased with large domain shift. To tackle this problem, we propose a novel end-to-end medical image segmentation model, namely Progressive Adversarial Semantic Segmentation (PASS), which can make improved segmentation predictions without requiring any domain-specific data during training time. Our extensive experimentation with 8 public diabetic retinopathy and chest X-ray datasets, confirms the effectiveness of PASS for accurate vascular and pulmonary segmentation, both for in-domain and cross-domain evaluations.

Index Terms—segmentation, adversarial learning, domain-shift, diabetic retinopathy, chest X-ray, lung, retinal vessels

I. INTRODUCTION

Deep learning-based image segmentation methods perform well amid the availability of large pools of labeled data. An important assumption underlying the success of deep convolutional neural networks is that the training data are sampled iid (independent, identical distribution). However, in real world scenarios, that assumption may not hold. By breaking the iid assumption, deep learning models can achieve robustness across different data domains.

Unlike the availability of natural image datasets, where the success of deep learning is mainly due to large training set [1], due to privacy issues and the scarcity of manual annotations, medical imaging datasets available for training are usually modest in size. Moreover, the problem is exacerbated due to the under-representation of some rare medical conditions, varying imaging configurations, modalities, among other factors (Fig. 1). This leads to the domain shift problem—when a model trained on data from one source does not generalize well or fails to predict proper segmentation for data from a different source. In that case, very non-intuitive and error-prone segmentations can be generated, even by the most sophisticated deep learning models [2], [3]. Thus training CNNs on medical imaging data for segmentation tasks lacks robustness when the iid assumption breaks, and they make terrible mistakes for ood (out of distribution) predictions.

Domain shift is usually tackled through unsupervised domain adaptation, where cross-domain data are required at training time [4], [5], [6]. Domain generalization is another approach that tries to learn a common representation for the data

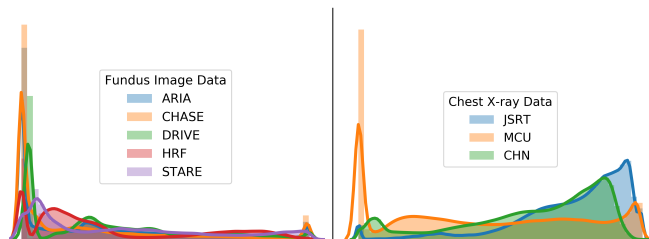


Fig. 1. Disparity in distributions of the datasets used in our experiments.

from both source and target domains. However, the additional unlabeled data required from the target domain are not readily available. Moreover, such approaches are not clinically viable due to their scaling issues across many target domains. A cost-effective solution is interactive segmentation, guided by experts in the loop. However, because of the manual intervention in the segmentation process, these approaches are not methodically feasible [7]. An end-to-end and elegant solution would not rely on manual intervention nor require training data from target domains.

Contributions: We introduce Progressive Adversarial Semantic Segmentation, or PASS, a novel segmentation model that improves segmentation predictions by tackling domain shift and small sample size issues. Our specific contributions are: **1)** A novel semantic segmentation model with progressive side-supervision and adversarial learning for improved, shape-aware, and anatomically-consistent segmentation of medical images. **2)** Reduction of domain shift for state-of-the-art models

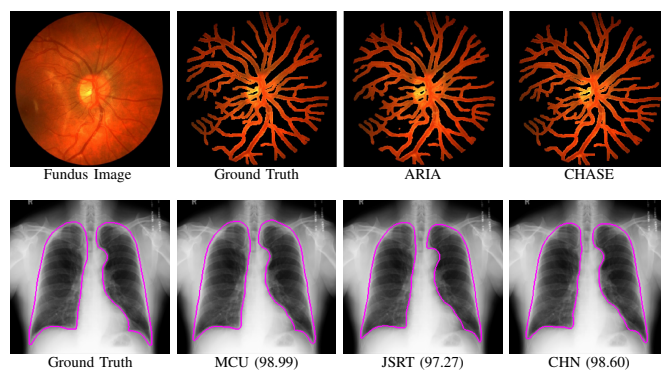


Fig. 2. Consistency of the in-domain and cross-domain segmentation predictions by our PASS model: (Top) Visualization of retinal vessel segmentation from a fundus image when trained on the ARIA and CHASE datasets. (Bottom) Segmentation of a chest X-ray from the MCU dataset when the model is trained on the MCU, JSRT, and CHN datasets.

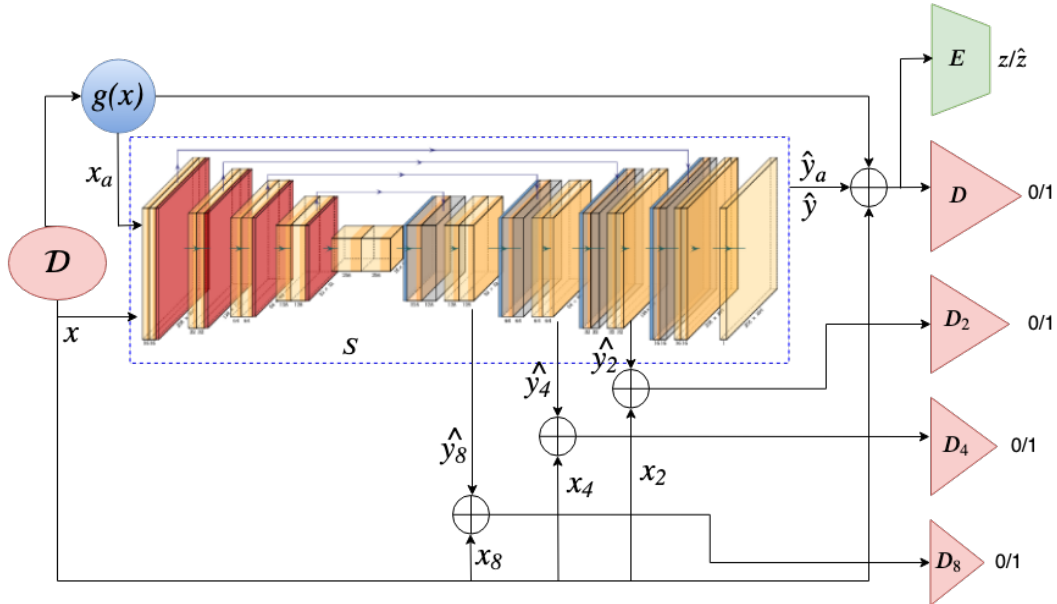


Fig. 3. Schematic of the PASS model: The segmentation mask generator S takes either input x or the transformed input x_a via a transformation function $g(x)$. The generated side outputs are passed to the corresponding discriminators D_2 , D_4 , and D_8 and the final outputs y_a/\hat{y} are passed to the discriminator D . The shape encoder E also takes y/\hat{y} as input to get the latent vector z/\hat{z} .

in small training data, with improved segmentation prediction in both in-domain and cross-domain evaluations. **3)** Extensive experimentation and statistical analyses with retinal fundus and chest X-ray image datasets, demonstrating the effectiveness of the PASS model in vascular and pulmonary segmentation (Fig. 2).

II. RELATED WORK

The following five topics are relevant to the present work: semi-supervised learning, adversarial learning, domain adaptation, prior-/post-processing segmentation, and error correction.

Semi-supervised models are evaluated by retaining only a portion of the labels from a dataset while the remainder are treated as unlabeled data [8]. Semi-supervised learning can be performed in at least two different ways—self-supervised and adversarial learning. Tajbakhsh *et al.* [9] showed the effectiveness of training models from pre-trained surrogate tasks in lung lobe segmentation with limited labeled data. Adversarial learning can effectively be adapted to semi-supervised learning for the classification of medical images [10]. Adversarial learning has also been utilized in segmentation (semantic-aware generative adversarial nets [11], structure correcting adversarial nets [12], etc.). We proposed a semi-supervised multitasking model with adversarial training [13]. Domain adaption can also be performed to learn a generic representation where the model is fully-supervised for source data and unsupervised for the target data [14]. These methods are typically reliant on the availability of unlabeled [15], [16] or even labeled data [17], [18] for the target domain. Therefore, with the unavailability of labeled/unlabeled data from the target domains or disparate data distributions, such models become less useful. Post-processing approaches inconsistently improve segmentation results but

require extensive parameter tuning [19] and error propagations before the post-processing [20]. ErrorNet is another method proposed recently that can learn error correction in a systematic manner via learning a prior distribution of the segmentation masks [21]. However, all of these methods are based on explicit error propagation whether it is handcrafted or model-derived. This adds vulnerability to the models for segmentation prediction and might increase shifts across different application tasks.

Departing from all the previous methods, PASS is end-to-end and fully automatic, devoid of any pre- or post-processing and explicit error-designs (handcrafted/systematic), and, most importantly, better generalized for filling domain gaps.

III. PASS

To formulate the problem, we assume an unknown data distribution $p(X, Y)$ over images and segmentation labels. The model has access to the labeled training set \mathcal{D} , and unlabeled set \mathcal{D}_A through on-the-fly transformation from $p(X)$ after marginalizing out Y . We set the learning objectives for the segmentation task as:

$$\min_{\psi, \phi, \theta} \mathcal{L}_{\mathcal{L}}(\mathcal{D}, (\psi, \phi, \theta)) + \lambda \mathcal{L}_{\mathcal{A}}(\mathcal{D}_A, (\psi, \phi, \theta)), \quad (1)$$

where the supervised objective $\mathcal{L}_{\mathcal{L}}$ is defined on the labeled data and the unsupervised objective $\mathcal{L}_{\mathcal{A}}$ is defined on the unlabeled data, λ is a non-negative weight parameter, and ψ , ϕ , and θ denote the parameters of the segmentor S , discriminator D , and encoder E networks, respectively.

A. Architecture Details

Fig. 3 illustrates the PASS model. PASS is based on the backbone of a progressive U-Net with some careful adjust-

Algorithm 1 PASS Training.

Require:

Training set of labeled data $x, y \in \mathcal{D}$
Transformation function $g(x)$ to generate x_a from x
Network architecture $S_\phi, D_\psi, E_\theta \in \mathcal{F}_{(\phi, \psi, \theta)}$ with learnable parameters ϕ, ψ, θ

for each epoch over \mathcal{D} **do**

Generate minibatches of unlabeled inputs \mathcal{M}_A using $g(x)$:
 $x_a = g(x)$

for each step **do**

Sample minibatch \mathcal{M} : $x_{(i)}; x_{(1)}, \dots, x_{(m)} \sim p_{\mathcal{D}(x)}$

Compute model outputs for the labeled inputs:

$$\hat{y} \leftarrow \mathcal{F}_{\phi, \psi, \theta}(\mathcal{M})$$

Compute model outputs for the unlabeled inputs:

$$\hat{y}_a \leftarrow \mathcal{F}_{\phi, \psi, \theta}(\mathcal{M}_A)$$

Update the discriminators $D_i (i = 1, \dots, d)$ along their gradients:

$$\nabla_{\psi_{D_i}} \frac{1}{|\mathcal{M}|} \sum_{i \in \mathcal{M}} \left[L_{D_i}(x_{(i)}, y_{(i)}, \hat{y}_{(i)}) \right] + \alpha \frac{1}{|\mathcal{M}_A|} \sum_{i \in \mathcal{M}_A} \left[L_{D_i}(x_{a_{(i)}}, \hat{y}_{a_{(i)}}) \right].$$

Update the shape encoder E along its gradient:

$$\nabla_{\theta_E} \frac{1}{|\mathcal{M}|} \sum_{i \in \mathcal{M}} \left[L_E(x_{(i)}, y_{(i)}, \hat{y}_{(i)}) \right].$$

Update the segmentation mask generator S along its gradient:

$$\nabla_{\phi_S} \frac{1}{|\mathcal{M}|} \sum_{i \in \mathcal{M}} \left[L_S(y_{(i)}, \hat{y}_{(i)}) \right] + \alpha \frac{1}{|\mathcal{M}_A|} \sum_{i \in \mathcal{M}_A} \left[L_S(y_{(i)}, \hat{y}_{a_{(i)}}) \right].$$

end for
end for

ments in the U-Net with side-adversary and side-supervision capabilities. As in a U-Net [22], PASS has a segmentor (S) with skip connections in an encoder-decoder architecture. In each encoder layer, two 3×3 convolutions are followed by instance normalization, leaky-ReLU activation, and a 2×2 max-pooling. We generate side-outputs in every stage of the decoder. The side-outputs are collected at the resolutions of $x/8$, $x/4$, and $x/2$ before the final output at the resolutions of x . According to the shape of the side-outputs, discriminators are employed and layers are added progressively. Progressively adding one side-output to the next improves the segmentation performance compared to collecting the output from the final decoder stage [2]. The progressive side-outputs also ensure that the network does not lose track of objects of interest. Moreover, progressively growing the discriminators enables the model to receive feedback at different resolutions via the side-outputs. While the discriminators are employed at different side-outputs, the segmentor tries to generate side-outputs closer to the ground truths progressively for an improved and accurate final segmentation. A shape encoder E is used in PASS

to match the latent representation of the stacked input and output of S with the stacked input and reference so that the model becomes shape-aware while mapping an input to the segmentation mask. Moreover, during training, a transformation function is used to obtain x_a from input x , and PASS makes a segmentation prediction on x_a . Note that x_a is used without any corresponding label information. Through this, PASS can be trained to make predictions on more diverse data crucial for evaluation in other domains.

B. Loss Functions

The three networks S , D , and E in the PASS model, are trained on separate objectives, according to Algorithm 1:

a) Segmentor Loss: The objective of segmentor S is based on the segmentation maps generated in different resolutions. We chose Dice loss to penalize the model for the segmentation map predictions. Therefore, the objective of S includes segmentation loss as a weighted sum of all the side-output and side-adversarial losses, where S wants the discriminators D_i to maximize the likelihood for the predicted segmentations. For the segmentation predictions, we employ Dice losses and the final loss is calculated as $\mathcal{L}_{S_{seg}} = \sum_i^4 w_i \mathcal{L}(y_i, \hat{y}_i)$. A second segmentation loss term is used for logit-wise distribution comparison. Since x_a is not paired with any reference segmentations, it is not possible to directly compare segmentation loss. Rather, we employ Kullback-Leibler (KL) divergence to penalize S for not maintaining the distribution of the predicted segmentation of the labeled data. The KL loss is calculated as

$$\mathcal{L}_{SKL} = \sum_i^{m^2} \left| (\hat{y}_{pk}(i) - \hat{y}_{a_{pk}}(i)) \log(y_{pk}(i) / \hat{y}_{a_{pk}}(i)) \right|. \quad (2)$$

Then, the segmentor's adversarial loss is calculated from the stacked input image and predicted segmentation when S wants D to maximize the likelihood as

$$\mathcal{L}_{S_{pred}(x_i, \hat{y}_i)} = -\mathbb{E}_{x_i, \hat{y}_i \sim S} \log[1 - D_i(x_i, \hat{y}_i)]. \quad (3)$$

Since the main objective of the segmentor is to generate the segmentation map, $\mathcal{L}_{S_{pred}}$ is usually weighed using a small number α . In addition, a feature loss is calculated by collecting intermediate convolutions from the discriminators. The goal of feature matching is to push S to generate segmentations that match reference data statistics. It is natural that D can find the most discriminative features. The feature loss across all the discriminators is calculated and summed as

$$\mathcal{L}_{S_{feature}} = \sum_i^d \|f_{x, y \sim \mathcal{D}}(x_i, y_i) - f_{x, \hat{y} \sim S}(x_i, \hat{y}_i)\|_2^2. \quad (4)$$

b) Discriminator Loss: The discriminator has only unsupervised loss objectives. When the model receives the stacked input image and reference segmentation label (x, y) from two different sources, the unsupervised loss contains the original adversarial loss for real data:

$$\mathcal{L}_{D_{i_{real}}} = -\mathbb{E}_{x_i, y_i \sim p_{data}} \log[1 - D_i(x_i, y_i)]. \quad (5)$$

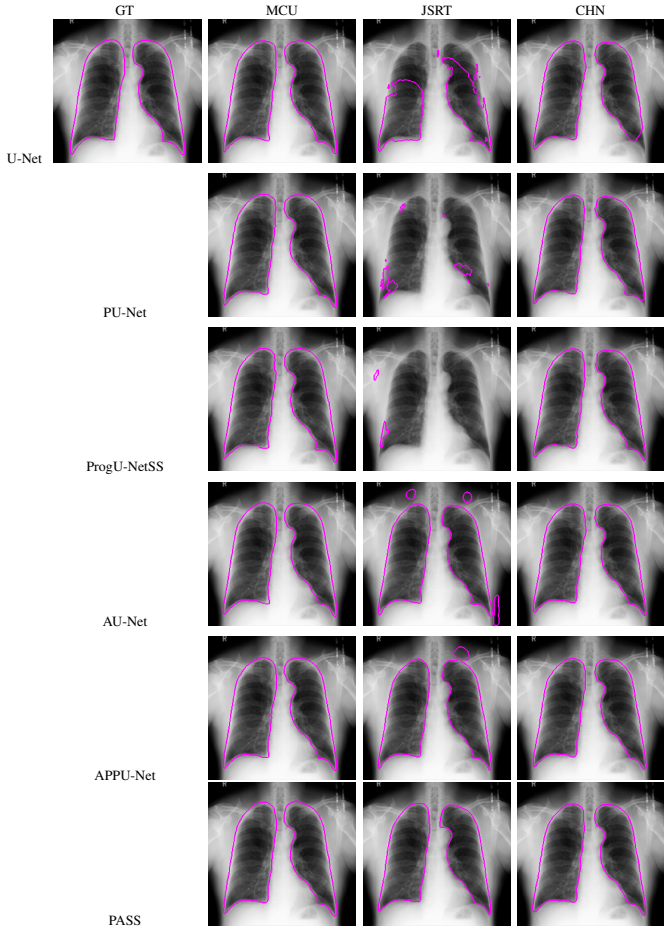


Fig. 4. Visualization of lung boundaries for the predicted segmentations of a chest X-Ray image from the MCU dataset when trained on the MCU, JSRT, and CHN datasets.

Similarly, the adversarial loss for predicted data is calculated from the stacked input image and predicted segmentation label x, \hat{y} as follows:

$$\mathcal{L}_{D_{i_{pred}}} = -\mathbb{E}_{(x_i, \hat{y}_i) \sim S} \log[D_i(x_i, \hat{y}_i)]. \quad (6)$$

c) Encoder Loss: The encoder is trained on matching the shapes of the predicted masks with the reference masks. The encoder E is fed with both the reference mask and the predicted mask, and their latent representations are acquired as the outputs. The encoder loss is simply the mean-square error between the two latent representations:

$$\mathcal{L}_E = \frac{1}{n} \sum_i^n \|z - \hat{z}\|^2, \quad (7)$$

where z is the latent vector representation of the reference segmentation and \hat{z} is the latent vector representation of the predicted segmentation.

IV. EMPIRICAL EVALUATION

A. Dataset, Implementation, and Other Details

a) Dataset: We validate our PASS model in two different experimental settings: vessel segmentation in diabetic retinopathy images and segmentation of lungs in chest X-ray images.

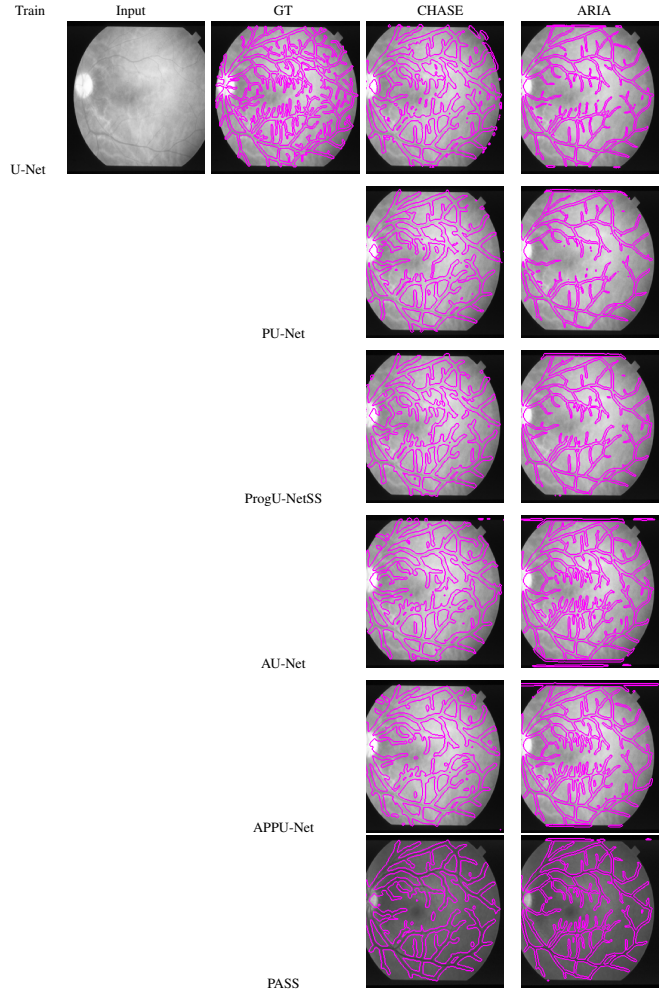


Fig. 5. Visualization of vascular segmentation from fundoscopic image from the STARE dataset when the models are trained on the CHASE and ARIA datasets.

TABLE I
PARTITIONING OF THE FUNDOSCOPIC AND CHEST X-RAY DATASETS USED IN OUR EXPERIMENTS.

Dataset	#Fundus images			Data splits			Dataset	#X-ray images			Data splits		
	Total	Healthy	Diseased	Train	Val	Test		Total	Healthy	Diseased	Train	Val	Test
DRIVE	40	33	7	18	2	20	MCU	138	80	58	93	10	35
STARE	20	10	10	10	2	8	JSRT	247	93	154	111	13	123
CHASE	28	20	8	17	5	6	CHN	566	279	287	377	43	142
ARIA	143	61	82	121	5	17							
HRF	45	15	30	26	5	14							

For former task, we used five publicly available fundus image datasets—ARIA [23], CHASE [24], DRIVE [25], STARE [26], and HRF [27]—with varying number of healthy and diseased images, and for the latter task, we used three public datasets—MCU, JSRT [28], and CHN [29]. Table I details the partitioning of the datasets in each application.

b) Inputs: All the images are resized and normalized to $256 \times 256 \times 3$ for the retinal images and $256 \times 256 \times 1$ for the chest X-rays before feeding them to the network.

c) Hyperparameters: We use the Adam optimizer with adaptive learning rate starting with initial rates of 0.01 for S ,

TABLE II
COMPARISON BETWEEN PASS AND OTHER PERFORMANCE BASELINES FOR RETINAL VESSEL SEGMENTATION (DICE SCORE). GREY COLUMNS INDICATE IN-DOMAIN AND WHITE COLUMNS INDICATE CROSS-DOMAIN EVALUATIONS.

Model	Train on →		CHASE					ARIA						
	Test on →		CHASE	DRIVE	ARIA	STARE	HRF	Avg.	CHASE	DRIVE	ARIA	STARE	HRF	Avg.
U-Net [22]			80.40	63.20	64.50	66.76	63.82	67.74	76.70	77.30	72.00	71.28	72.30	73.90
U-Net+CRF [21]			81.20	65.40	62.60	56.40	63.60	65.80	78.40	69.50	73.00	64.60	73.50	71.80
PU-Net [30]			81.58	64.04	63.03	66.20	62.66	67.50	76.7	77.3	72.0	71.28	72.3	73.9
AttnU-Net [31]			81.37	65.23	62.91	64.28	65.72	67.90	76.7	77.3	72.0	71.28	72.3	73.9
ProgU-Net [32]			82.91	61.02	63.28	66.58	63.43	67.44	47.21	64.54	70.56	66.57	60.17	61.81
ProgU-NetSS [13]			80.16	62.13	62.41	65.44	63.78	66.78	57.96	65.93	74.47	69.08	60.08	65.50
V-GAN [33]			79.70	71.50	64.20	61.00	66.40	68.50	68.70	75.80	69.90	66.20	69.30	70.00
AU-Net [34]			82.20	63.20	61.84	67.17	63.37	67.56	68.06	70.21	78.12	74.95	69.69	72.21
APPU-Net [13]			82.58	62.50	61.22	66.17	62.60	67.01	66.20	69.68	78.48	76.34	69.31	72.00
UDA [35]			72.30	69.30	68.20	64.70	67.40	68.40	71.50	72.90	73.20	71.30	70.70	71.90
ErrorNet [21]			81.50	73.20	66.50	65.20	68.60	71.00	76.70	78.90	72.00	74.00	72.60	74.80
PASS without $g(x)$			89.06	80.76	80.72	82.72	75.26	81.70	85.06	88.14	91.92	90.78	82.62	87.70
PASS			91.96	84.96	84.18	86.84	78.57	85.30	86.32	90.55	92.08	91.50	83.15	88.72

TABLE III
COMPARISON BETWEEN PASS AND OTHER PERFORMANCE BASELINES FOR LUNG SEGMENTATION FROM CHEST X-RAY IMAGES (DICE SCORE). GREY COLUMNS INDICATE IN-DOMAIN EVALUATION AND WHITE COLUMNS INDICATE CROSS-DOMAIN EVALUATIONS.

Model	Train on →		MCU				JSRT				CHN			
	Test on →		MCU	JSRT	CHN	Avg.	MCU	JSRT	CHN	Avg.	MCU	JSRT	CHN	Avg.
U-Net [22]			97.67	39.39	94.48	77.18	92.00	95.02	90.54	92.58	93.72	43.46	95.84	77.67
PU-Net [30]			97.89	21.24	97.84	72.33	84.97	94.94	73.68	84.53	93.57	73.88	95.90	87.78
AttnU-Net [31]			97.86	30.31	94.07	74.08	6.70	94.95	65.00	55.55	81.25	74.24	95.56	83.68
ProgU-Net [32]			97.83	10.98	91.32	66.71	34.89	95.20	86.28	72.12	84.79	60.03	95.35	80.06
ProgU-NetSS [13]			97.90	33.98	95.32	75.33	13.16	95.09	65.00	57.75	94.24	67.29	95.63	85.72
AU-Net [34]			97.86	94.68	95.08	95.87	89.12	97.85	92.46	93.14	95.58	95.88	96.22	95.89
APPU-Net [13]			97.81	95.07	94.77	95.88	90.46	97.80	91.76	93.34	95.72	96.25	96.11	96.03
CyUDA [11]			95.61	92.84	-	94.23	-	-	-	-	-	-	-	-
SeUDA [11]			95.61	94.51	-	--	-	-	-	-	-	-	-	-
CoDAGAN [36]			-	-	-	-	84.58	96.45	88.99	90.01	-	-	-	-
PASS without $g(x)$			97.74	96.43	96.76	96.98	95.11	98.26	95.92	96.43	96.62	96.11	97.61	96.68
PASS			98.22	96.56	97.24	97.34	95.70	98.27	96.06	96.68	97.27	97.15	97.65	97.36

and 0.001 for D and E . The learning rates are decreased 90% after every 5 epochs with exponential decay. We apply the dropout with a rate of 0.25. We use $\lambda = 0.3$ for weighting \mathcal{L}_A and $\alpha = 0.01$ in (3).

d) Machine Configuration: We implemented PASS in Tensorflow on a Nvidia Titan V GPU and a 64-bit Intel(R) Core(TM) i7-9700K CPU.

e) Evaluation: Along with qualitative visualization of segmentation masks and edges overlaid on the original input images, we use the Dice score (DS), structural similarity index (SSIM), and average Hausdorff distance (HD).

f) Baselines: We employ a number of baseline and state-of-the-art models for medical image segmentation and domain adaptation.¹

B. Results

As reported in Tables II and III, PASS outperforms all the baselines and state-of-the-art models for both retinal vessel and lung segmentation tasks.

¹U-Net, U-Net with CRF, Pyramid U-Net (PU-Net), Progressive U-Net (ProgU-Net), Attention U-Net (AttnU-Net), Progressive U-Net with Side-Supervision (ProgU-NetSS), Adversarial U-Net (AU-Net), V-GAN, Adversarial Pyramid Progressive U-Net (APPU-Net), Unsupervised Domain Adaptation (UDA), ErrorNet, and Conditional Domain Adaptation with GAN (CoDAGAN).

TABLE IV
COMPARISON BETWEEN PASS AND OTHER PERFORMANCE BASELINES FOR PULMONARY SEGMENTATION (HD SCORE). GREY COLUMNS INDICATE IN-DOMAIN AND WHITE COLUMNS INDICATE CROSS-DOMAIN EVALUATIONS.

Model	Train on →				MCU				JSRT				CHN			
	Test on →				MCU	JSRT	CHN	Avg.	MCU	JSRT	CHN	Avg.	MCU	JSRT	CHN	Avg.
U-Net					3.689	9.948	4.849	6.162	7.923	4.128	5.594	5.882	4.874	9.161	4.378	6.138
PU-Net					3.723	11.049	5.346	6.706	10.926	4.159	6.618	7.234	5.347	7.438	4.362	5.716
AttnU-Net					3.841	10.189	5.057	6.362	11.628	4.181	7.374	7.728	6.989	7.257	4.453	6.233
ProgU-Net					3.729	11.706	5.564	6.999	10.491	4.052	5.700	6.748	6.788	8.702	4.494	6.661
ProgU-NetSS					3.874	9.907	4.673	6.151	11.602	4.117	7.509	7.743	4.885	7.906	4.362	5.718
AU-Net					3.780	4.625	4.651	4.352	4.879	3.705	5.126	4.570	4.327	4.499	4.301	4.376
APPU-Net					3.736	4.537	4.725	4.333	4.732	3.706	5.055	4.498	4.485	4.278	4.401	4.388
PASS without $g(x)$					3.332	4.552	4.857	4.247	5.109	3.867	5.138	4.705	4.580	4.441	4.545	4.522
PASS					3.262	3.996	4.675	3.978	4.680	3.702	5.021	4.468	4.269	4.397	4.112	4.259

TABLE V
COMPARISON BETWEEN PASS AND OTHER PERFORMANCE BASELINES FOR PULMONARY SEGMENTATION (SSIM SCORE). GREY COLUMNS INDICATE IN-DOMAIN AND WHITE COLUMNS INDICATE CROSS-DOMAIN EVALUATIONS.

Model	Train on →				MCU				JSRT				CHN			
	Test on →				MCU	JSRT	CHN	Avg.	MCU	JSRT	CHN	Avg.	MCU	JSRT	CHN	Avg.
U-Net					0.968	0.754	0.935	0.886	0.803	0.949	0.908	0.887	0.929	0.738	0.949	0.872
PU-Net					0.967	0.672	0.921	0.853	0.698	0.948	0.839	0.828	0.931	0.836	0.949	0.905
AttnU-Net					0.967	0.699	0.926	0.864	0.679	0.948	0.820	0.816	0.869	0.837	0.946	0.884
ProgU-Net					0.968	0.656	0.919	0.848	0.732	0.951	0.889	0.857	0.886	0.837	0.946	0.889
ProgU-NetSS					0.968	0.716	0.941	0.875	0.689	0.949	0.828	0.822	0.934	0.822	0.948	0.901
AU-Net					0.967	0.9191	0.936	0.941	0.892	0.961	0.916	0.923	0.942	0.937	0.951	0.943
APPU-Net					0.967	0.922	0.934	0.941	0.902	0.960	0.913	0.925	0.944	0.940	0.950	0.945
PASS without $g(x)$					0.962	0.921	0.932	0.938	0.913	0.953	0.921	0.929	0.939	0.931	0.945	0.938
PASS					0.968	0.923	0.942	0.944	0.918	0.955	0.920	0.931	0.942	0.939	0.956	0.946

In vessel segmentation, PASS achieved an overall average Dice score of 85.30 and cross-domain score of 83.74 (domain gap of 8.32), when trained on the small CHASE dataset. When trained on the relatively larger ARIA dataset, the overall average Dice score of 88.72 and cross-domain score of 87.88 are achieved with domain gap of 4.22. This demonstrates the effectiveness of PASS across the domains as it is capable of performing the semantic segmentation with the ability to learn diversity in shapes and distributions. Similarly, in the segmentation of lungs, PASS outperformed all the baselines and state-of-the-art models (Table III).

Along with Fig. 2, Fig. 4 (edges) shows the consistency of PASS in segmenting lungs from the chest X-ray and Fig. 5 shows the consistency of PASS in segmenting retinal vessels from both in-domain and cross-domains irrespective of the varying imaging configurations and abnormalities. While some of the baseline models completely failed in evaluations on the JSRT dataset when trained on MCU and vice-versa, PASS consistently performs better in either scenario. With PASS, we have a domain gap of only 1.32 when trained on MCU, 2.39

when trained on JSRT, and 0.44 when trained on CHN. The poorer performance of the PASS model without $g(x)$ justifies the inclusion of this transformation function and the logit-wise distribution matching.

The HD and SSIM scores are reported for lung segmentation in Table IV and Table V, and for retinal vessel segmentation in Table VI and Table VII. The consistently lower HD scores and higher SSIM scores compared to the baselines provide further evidence of the superior performance of our PASS model.

V. CONCLUSIONS

We introduced PASS, a novel semantic segmentation model for intelligently mitigating the domain shift problem caused by small datasets. We evaluated PASS using 8 public datasets for the tasks of retinal vessel segmentation from diabetic retinopathy images and lung segmentation from chest X-ray images. Our experimental results demonstrated the effectiveness of PASS in both in-domain and cross-domain evaluations, even with smaller sample size and larger domain shift. Our future work will focus on evaluating PASS on other medical image

TABLE VI

COMPARISON BETWEEN PASS AND OTHER PERFORMANCE BASELINES FOR RETINAL VESSEL SEGMENTATION (AVERAGE HD SCORE). GREY COLUMNS INDICATE IN-DOMAIN AND WHITE COLUMNS INDICATE CROSS-DOMAIN EVALUATIONS.

Model	Train on →		CHASE					ARIA					
	Test on →	CHASE	DRIVE	ARIA	STARE	HRF	Avg.	CHASE	DRIVE	ARIA	STARE	HRF	Avg.
U-Net		7.929	8.306	7.490	7.807	8.916	8.089	9.177	8.095	6.404	7.209	9.017	7.980
PU-Net		7.287	8.260	7.526	7.551	8.815	7.887	9.381	8.247	6.905	7.420	9.403	8.271
AttnU-Net		7.436	8.515	7.672	7.899	8.982	8.100	9.765	8.297	7.186	7.691	9.543	8.496
ProgU-Net		7.233	8.408	7.613	7.850	9.000	8.021	9.400	8.144	6.627	7.316	9.133	8.124
ProgU-NetSS		7.498	8.478	7.560	8.055	9.012	8.121	8.857	8.072	6.478	7.089	9.143	7.928
AU-Net		7.406	8.482	7.665	7.792	8.946	8.058	8.508	7.770	6.448	6.606	8.510	7.568
APPU-Net		7.196	8.492	7.732	7.824	8.979	8.045	8.486	8.009	6.344	6.519	8.655	7.602
PASS without $g(x)$		7.154	7.809	7.397	7.346	8.261	7.593	8.349	8.132	6.301	6.120	8.074	7.396
PASS		7.129	7.341	7.187	7.745	8.028	7.486	8.285	8.012	6.336	6.123	7.399	7.231

TABLE VII

COMPARISON BETWEEN PASS AND OTHER PERFORMANCE BASELINES FOR RETINAL VESSEL SEGMENTATION (SSIM SCORE). GREY COLUMNS INDICATE IN-DOMAIN AND WHITE COLUMNS INDICATE CROSS-DOMAIN EVALUATIONS.

Model	Train on →		CHASE					ARIA					
	Test on →	CHASE	DRIVE	ARIA	STARE	HRF	Avg.	CHASE	DRIVE	ARIA	STARE	HRF	Avg.
U-Net		0.812	0.645	0.665	0.684	0.507	0.663	0.682	0.734	0.791	0.776	0.571	0.711
PU-Net		0.815	0.678	0.666	0.699	0.501	0.672	0.679	0.722	0.769	0.751	0.537	0.692
AttnU-Net		0.808	0.645	0.648	0.687	0.498	0.657	0.675	0.725	0.764	0.753	0.543	0.692
ProgU-Net		0.819	0.611	0.653	0.679	0.490	0.650	0.677	0.739	0.791	0.774	0.595	0.715
ProgU-NetSS		0.802	0.624	0.652	0.659	0.501	0.648	0.698	0.741	0.797	0.783	0.586	0.721
AU-Net		0.812	0.624	0.641	0.658	0.482	0.643	0.706	0.738	0.789	0.779	0.632	0.729
APPU-Net		0.820	0.619	0.636	0.654	0.484	0.643	0.695	0.738	0.796	0.789	0.632	0.730
PASS without $g(x)$		0.827	0.682	0.661	0.699	0.505	0.675	0.696	0.742	0.798	0.791	0.610	0.725
PASS		0.830	0.685	0.660	0.701	0.510	0.677	0.707	0.772	0.797	0.802	0.611	0.738

segmentation tasks as well as evaluating the effectiveness of PASS in iterative and continual learning scenarios.

REFERENCES

- [1] A. Krizhevsky, I. Sutskever, and G. E. Hinton, "Imagenet classification with deep convolutional neural networks," in *Advances in neural information processing systems*, 2012, pp. 1097–1105. 1
- [2] A.-A.-Z. Imran, A. Hatamizadeh, S. P. Ananth, X. Ding, D. Terzopoulos, and N. Tajbakhsh, "Automatic segmentation of pulmonary lobes using a progressive dense V-network," in *Deep Learning in Medical Image Analysis and Multimodal Learning for Clinical Decision Support*. Springer, 2018, pp. 282–290. 1, 3
- [3] Z. Zhou, M. M. R. Siddiquee, N. Tajbakhsh, and J. Liang, "Unet++: Redesigning skip connections to exploit multiscale features in image segmentation," *IEEE Transactions on Medical Imaging*, 2019. 1
- [4] Q. Dou, C. Chen, C. Ouyang, H. Chen, and P. A. Heng, "Unsupervised domain adaptation of convnets for medical image segmentation via adversarial learning," in *Deep Learning and Convolutional Neural Networks for Medical Imaging and Clinical Informatics*. Springer, 2019, pp. 93–115. 1
- [5] C. Chen, Q. Dou, H. Chen, J. Qin, and P. A. Heng, "Unsupervised bidirectional cross-modality adaptation via deeply synergistic image and feature alignment for medical image segmentation," *IEEE Transactions on Medical Imaging*, 2020. 1
- [6] Q. Dou, C. Ouyang, C. Chen, H. Chen, and P.-A. Heng, "Unsupervised cross-modality domain adaptation of convnets for biomedical image segmentations with adversarial loss," *arXiv preprint arXiv:1804.10916*, 2018. 1
- [7] T. Sakinis, F. Milletari, H. Roth, P. Korfiatis, P. Kostandy, K. Philbrick, Z. Akkus, Z. Xu, D. Xu, and B. J. Erickson, "Interactive segmentation of medical images through fully convolutional neural networks," *arXiv preprint arXiv:1903.08205*, 2019. 1
- [8] X. Zhai, A. Oliver, A. Kolesnikov, and L. Beyer, "S⁴l: Self-supervised semi-supervised learning," *arXiv preprint arXiv:1905.03670*, 2019. 2
- [9] N. Tajbakhsh, Y. Hu, J. Cao, X. Yan, Y. Xiao, Y. Lu, J. Liang, D. Terzopoulos, and X. Ding, "Surrogate supervision for medical image analysis: Effective deep learning from limited quantities of labeled data," in *Proc. IEEE International Symposium on Biomedical Imaging (ISBI'19)*, 2019, pp. 1251–1255. 2
- [10] H. Salehinejad, S. Valaee, T. Dowdell, E. Colak, and J. Barfett, "Generalization of deep neural networks for chest pathology classification in X-rays using generative adversarial networks," in *ICASSP*, 2018. 2
- [11] C. Chen, Q. Dou, H. Chen, and P.-A. Heng, "Semantic-aware generative adversarial nets for unsupervised domain adaptation in chest X-ray segment," *arXiv:1806.00600*, 2018. 2, 5
- [12] W. Dai, N. Dong, Z. Wang, X. Liang, H. Zhang, and E. P. Xing, "SCAN: Structure correcting adversarial network for organ segmentation in chest X-rays," in *Deep Learning in Medical Image Analysis*, ser. LNCS, 2018, vol. 11045. 2
- [13] A.-A.-Z. Imran and D. Terzopoulos, "Semi-supervised multi-task learning with chest x-ray images," in *Machine Learning in Medical Imaging: 10th International Workshop, MLMI 2019, Held in Conjunction with MICCAI 2019, Shenzhen, China, October 13, 2019, Proceedings*, vol. 11861. Springer Nature, 2019, p. 151. 2, 5

- [14] J. Yang, N. C. Dvornik, F. Zhang, J. Zhuang, J. Chapiro, M. Lin, and J. S. Duncan, "Domain-agnostic learning with anatomy-consistent embedding for cross-modality liver segmentation," in *Proceedings of the IEEE International Conference on Computer Vision Workshops*, 2019. 2
- [15] C. Chen, Q. Dou, H. Chen, J. Qin, and P.-A. Heng, "Synergistic image and feature adaptation: Towards cross-modality domain adaptation for medical image segmentation," in *Proceedings of the AAAI Conference on Artificial Intelligence*, vol. 33, 2019, pp. 865–872. 2
- [16] Y. Huo, Z. Xu, H. Moon, S. Bao, A. Assad, T. K. Moyo, M. R. Savona, R. G. Abramson, and B. A. Landman, "Synseg-net: Synthetic segmentation without target modality ground truth," *IEEE transactions on medical imaging*, vol. 38, no. 4, pp. 1016–1025, 2018. 2
- [17] Z. Zhang, L. Yang, and Y. Zheng, "Translating and segmenting multimodal medical volumes with cycle-and shape-consistency generative adversarial network," in *Proceedings of the IEEE conference on computer vision and pattern recognition*, 2018, pp. 9242–9251. 2
- [18] Q. Dou, C. Ouyang, C. Chen, H. Chen, B. Glocker, X. Zhuang, and P.-A. Heng, "Pnp-adanet: Plug-and-play adversarial domain adaptation network with a benchmark at cross-modality cardiac segmentation," *arXiv preprint arXiv:1812.07907*, 2018. 2
- [19] K. Kamnitsas, C. Ledig, V. F. Newcombe, J. P. Simpson, A. D. Kane, D. K. Menon, D. Rueckert, and B. Glocker, "Efficient multi-scale 3d cnn with fully connected crf for accurate brain lesion segmentation," *Medical image analysis*, vol. 36, pp. 61–78, 2017. 2
- [20] A. J. Larrazabal, C. Martinez, and E. Ferrante, "Anatomical priors for image segmentation via post-processing with denoising autoencoders," in *International Conference on Medical Image Computing and Computer-Assisted Intervention*. Springer, 2019, pp. 585–593. 2
- [21] N. Tajbakhsh, B. Lai, S. Ananth, and X. Ding, "Errornet: Learning error representations from limited data to improve vascular segmentation," *arXiv preprint arXiv:1910.04814*, 2019. 2, 5
- [22] O. Ronneberger, P. Fischer, and T. Brox, "U-net: Convolutional networks for biomedical image segmentation," in *International Conference on Medical Image Computing and Computer-Assisted Intervention*. Springer, 2015, pp. 234–241. 3, 5
- [23] P. Bankhead, C. N. Scholfield, J. G. McGeown, and T. M. Curtis, "Fast retinal vessel detection and measurement using wavelets and edge location refinement," *PloS one*, vol. 7, no. 3, 2012. 4
- [24] M. M. Fraz, P. Remagnino, A. Hoppe, B. Uyyanonvara, A. R. Rudnicka, C. G. Owen, and S. A. Barman, "An ensemble classification-based approach applied to retinal blood vessel segmentation," *IEEE Transactions on Biomedical Engineering*, vol. 59, no. 9, pp. 2538–2548, 2012. 4
- [25] J. Staal, M. D. Abràmoff, M. Niemeijer, M. A. Viergever, and B. Van Ginneken, "Ridge-based vessel segmentation in color images of the retina," *IEEE transactions on medical imaging*, vol. 23, no. 4, pp. 501–509, 2004. 4
- [26] A. Hoover, V. Kouznetsova, and M. Goldbaum, "Locating blood vessels in retinal images by piecewise threshold probing of a matched filter response," *IEEE Transactions on Medical Imaging*, vol. 19, no. 3, pp. 203–210, 2000. 4
- [27] A. Budai, R. Bock, A. Maier, J. Hornegger, and G. Michelson, "Robust vessel segmentation in fundus images," *International journal of biomedical imaging*, vol. 2013, 2013. 4
- [28] J. Shiraishi, S. Katsuragawa, J. Ikezoe, T. Matsumoto, T. Kobayashi, K.-i. Komatsu, M. Matsui, H. Fujita, Y. Kodera, and K. Doi, "Development of a digital image database for chest radiographs with and without a lung nodule: receiver operating characteristic analysis of radiologists' detection of pulmonary nodules," *American Journal of Roentgenology*, vol. 174, no. 1, pp. 71–74, 2000. 4
- [29] S. Jaeger, S. Candemir, S. Antani, Y.-X. J. Wang, P.-X. Lu, and G. Thoma, "Two public chest x-ray datasets for computer-aided screening of pulmonary diseases," *Quantitative imaging in medicine and surgery*, vol. 4, no. 6, p. 475, 2014. 4
- [30] H. Fu, J. Cheng, Y. Xu, D. W. K. Wong, J. Liu, and X. Cao, "Joint optic disc and cup segmentation based on multi-label deep network and polar transformation," *IEEE transactions on medical imaging*, vol. 37, no. 7, pp. 1597–1605, 2018. 5
- [31] O. Oktay, J. Schlemper, L. L. Folgoc, M. Lee, M. Heinrich, K. Misawa, K. Mori, S. McDonagh, N. Y. Hammerla, B. Kainz *et al.*, "Attention u-net: Learning where to look for the pancreas," *arXiv preprint arXiv:1804.03999*, 2018. 5
- [32] A.-A.-Z. Imran, C. Huang, H. Tang, W. Fan, K. M. Cheung, M. To, Z. Qian, and D. Terzopoulos, "End-to-end fully automatic segmentation of scoliotic vertebrae in spinal X-ray images," in *Medical Imaging Meets NeurIPS Workshop*, Vancouver, Canada, December 2019. 5
- [33] J. Son, S. J. Park, and K.-H. Jung, "Retinal vessel segmentation in fundoscopic images with generative adversarial networks," *arXiv preprint arXiv:1706.09318*, 2017. 5
- [34] S. Izadi, Z. Mirikharaji, J. Kawahara, and G. Hamarneh, "Generative adversarial networks to segment skin lesions," in *2018 IEEE 15th International Symposium on Biomedical Imaging (ISBI 2018)*. IEEE, 2018, pp. 881–884. 5
- [35] N. Dong, M. Kampffmeyer, X. Liang, Z. Wang, W. Dai, and E. Xing, "Unsupervised domain adaptation for automatic estimation of cardiothoracic ratio," in *International conference on medical image computing and computer-assisted intervention*. Springer, 2018, pp. 544–552. 5
- [36] H. Oliveira, E. Ferreira, and J. A. d. Santos, "Truly generalizable radiograph segmentation with conditional domain adaptation," *arXiv preprint arXiv:1901.05553*, 2019. 5

SUPPLEMENTARY MATERIAL

TABLE VIII
ARCHITECTURAL DETAILS OF THE SHAPE ENCODER (E)

Name	Feature maps (input)	Feature maps (output)
Conv layer - 1a	$256 \times 256 \times 3$	$256 \times 256 \times 16$
Conv layer - 1b	$256 \times 256 \times 16$	$256 \times 256 \times 16$
Max pool - 1	$256 \times 256 \times 16$	$128 \times 128 \times 16$
Conv layer - 2a	$128 \times 128 \times 16$	$128 \times 128 \times 32$
Conv layer - 2b	$128 \times 128 \times 32$	$128 \times 128 \times 32$
Max pool - 2	$128 \times 128 \times 32$	$64 \times 64 \times 32$
Conv layer - 3a	$64 \times 64 \times 32$	$64 \times 64 \times 64$
Conv layer - 3b	$64 \times 64 \times 64$	$64 \times 64 \times 64$
Max pool - 3	$64 \times 64 \times 64$	$32 \times 32 \times 64$
Conv layer - 4a	$32 \times 32 \times 64$	$32 \times 32 \times 128$
Conv layer - 4b	$32 \times 32 \times 128$	$32 \times 32 \times 128$
Max pool - 4	$32 \times 32 \times 128$	$16 \times 16 \times 128$
Conv layer - 5a	$16 \times 16 \times 128$	$16 \times 16 \times 256$
Conv layer - 5b	$16 \times 16 \times 256$	$16 \times 16 \times 256$
encoder flatten - 5	$16 \times 16 \times 256$	65536
encoder dense - z	65536	256

TABLE IX
ARCHITECTURAL DETAILS OF THE DISCRIMINATOR (D)

Name	Feature maps (input)	Feature maps (output)
Conv layer - 1a	$256 \times 256 \times 3$	$256 \times 256 \times 16$
Conv layer - 1b	$256 \times 256 \times 16$	$256 \times 256 \times 16$
Max pool - 1	$256 \times 256 \times 16$	$128 \times 128 \times 16$
Conv layer - 2a	$128 \times 128 \times 16$	$128 \times 128 \times 32$
Conv layer - 2b	$128 \times 128 \times 32$	$128 \times 128 \times 32$
Max pool - 2	$128 \times 128 \times 32$	$64 \times 64 \times 32$
Conv layer - 3a	$64 \times 64 \times 32$	$64 \times 64 \times 64$
Conv layer - 3b	$64 \times 64 \times 64$	$64 \times 64 \times 64$
Max pool - 3	$64 \times 64 \times 64$	$32 \times 32 \times 64$
Conv layer - 4a	$32 \times 32 \times 64$	$32 \times 32 \times 128$
Conv layer - 4b	$32 \times 32 \times 128$	$32 \times 32 \times 128$
Max pool - 4	$32 \times 32 \times 128$	$16 \times 16 \times 128$
discriminator flatten - 4	$16 \times 16 \times 128$	32768
discriminator dense - l	32768	1

TABLE X
ARCHITECTURAL DETAILS OF THE DISCRIMINATOR (D_2)

Name	Feature maps (input)	Feature maps (output)
Conv layer - 1a	$128 \times 128 \times 3$	$128 \times 128 \times 32$
Conv layer - 1b	$128 \times 128 \times 32$	$128 \times 128 \times 32$
Max pool - 1	$128 \times 128 \times 32$	$64 \times 64 \times 32$
Conv layer - 2a	$64 \times 64 \times 32$	$64 \times 64 \times 64$
Conv layer - 2b	$64 \times 64 \times 64$	$64 \times 64 \times 64$
Max pool - 2	$64 \times 64 \times 64$	$32 \times 32 \times 64$
Conv layer - 3a	$32 \times 32 \times 64$	$32 \times 32 \times 128$
Conv layer - 3b	$32 \times 32 \times 128$	$32 \times 32 \times 128$
Max pool - 3	$32 \times 32 \times 128$	$16 \times 16 \times 128$
discriminator flatten - 3	$16 \times 16 \times 128$	32768
discriminator dense - l	32768	1

TABLE XI
ARCHITECTURAL DETAILS OF THE DISCRIMINATOR (D_4)

Name	Feature maps (input)	Feature maps (output)
Conv layer - 1a	$64 \times 64 \times 3$	$64 \times 64 \times 64$
Conv layer - 1b	$64 \times 64 \times 64$	$64 \times 64 \times 64$
Max pool - 1	$64 \times 64 \times 64$	$32 \times 32 \times 64$
Conv layer - 2a	$32 \times 32 \times 64$	$32 \times 32 \times 128$
Conv layer - 2b	$32 \times 32 \times 128$	$32 \times 32 \times 128$
Max pool - 2	$32 \times 32 \times 128$	$16 \times 16 \times 128$
discriminator flatten - 2	$16 \times 16 \times 128$	32768
discriminator dense - l	32768	1

TABLE XII
ARCHITECTURAL DETAILS OF THE DISCRIMINATOR (D_8)

Name	Feature maps (input)	Feature maps (output)
Conv layer - 1a	$32 \times 32 \times 3$	$32 \times 32 \times 128$
Conv layer - 1b	$32 \times 32 \times 128$	$32 \times 32 \times 128$
Max pool - 1	$32 \times 32 \times 128$	$16 \times 16 \times 128$
discriminator flatten - 1	$16 \times 16 \times 128$	32768
discriminator dense - l	32768	1